International Journal of Applied Earth Observation and Geoinformation 122 (2023) 103450

Contents lists available at ScienceDirect

International Journal of Applied Earth Observation and Geoinformation

journal homepage: www.elsevier.com/locate/jag

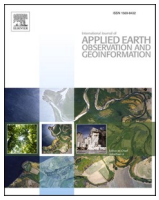

Seismic urban damage map generation based on satellite images and Gabor convolutional neural networks

Heidar Rastiveis [a,b,*], Seyd Teymoor Seydi [a], ZhiQiang Chen [c], Jonathan Li [d]

[a] Dept. of Photogrammetry and Remote Sensing, School of Surveying and Geospatial Engineering, University of Tehran, Tehran, Iran
[b] Lyles School of Civil Engineering, Purdue University, West Lafayette, USA
[c] School of Science and Engineering, University of Missouri-Kansas City, USA
[d] Departments of Geography and Environmental Management and Systems Design Engineering, University of Waterloo, 200 University Avenue West, Waterloo, Ontario N2L 3G1, Canada

ARTICLE INFO

Keywords:
Remote sensing
Earthquake
Buildings
Roads
Damage
Deep learning
Conventional Neural Network
Gabor Filter

ABSTRACT

Rapid assessment of urban damages after a strong earthquake is a necessary and crucial task to reduce the number of fatalities and recover socioeconomic services. In this paper, a novel deep-learning-based framework is proposed for detecting and mapping damages in urban buildings and roads using post-earthquake high-resolution satellite imagery. The method begins with overlaying a pre-event vector map on an input image to extract the building and road objects. The core machine learning components include two separate convolutional neural networks (CNN), integrated with Gabor filters, which extract debris pixels associated with building and road objects. These debris pixels are analyzed to generate the final damage maps, which show multiple damage degrees for buildings and roads. Two different datasets were used to thoroughly evaluate the proposed method's overall effectiveness. The overall accuracy of 95% for detecting the debris pixels in building and road areas proves the effectiveness of the proposed CNN models for debris detection in comparison to the traditional Machine Learning (ML) methods. The proposed method successfully labelled 84% of the buildings and 87% of the roads when compared with a manually generated multiple damage map.

1. Introduction

1.1. Motivation

Earthquakes are known as one of the most deadly and catastrophic natural hazards on earth. Among the death tolls, many were directly lost due to building damages or collapses (e.g., residential or commercial buildings) (Lu et al., 2023). Some damages were indirectly attributed to disabled functionalities of lifeline infrastructure. Indirect loss of lives in the aftermath of strong earthquakes may be caused by disrupted services of medical facilities due to impassable road networks. Besides claiming lives and injuries, earthquakes threaten all aspects of human societies, including social, economic, and technical activities (Bellini et al., 2023). On the other hand, these activities are physically supported by civil structures and lifeline infrastructure, including road networks. Therefore, rapid and accurate mapping of damaged buildings and road networks in urban areas is necessary to provide decision support for immediate post-earthquake rescue and long-term recovery of critical functionalities of societies (Rastiveis et al., 2013).

Various remote sensing (RS) technologies and data sources, such as high-resolution optical images, have been used for damage map generation (Irwansyah and Gunawan, 2023). Due to the increasing spatial resolution and availability during the last two decades, optical satellite images have been popularly adopted for urban damage detection and mapping (Tiwari et al., 2023). Several machine learning (ML)- and deep learning (DL)-based methods have been proposed for detecting damaged buildings or blocked roads after earthquake using satellite imagery. In the majority of these methods, debris pixels were often treated as the most visually salient feature in satellite images. However, nearly all these damage detection methods have focused on either buildings or roads, and none of them have conducted the two detection problems considering their intrinsic relation, as road blockage is mainly due to structural debris that further comes from building damages. Besides, DL algorithms have recently emerged as the fastest-growing trend in satellite image understanding. Therefore, in this paper we propose a state-of-the-art DL-based method for damage assessment using satellite

* Corresponding author at: Dept. of Photogrammetry and Remote Sensing, School of Surveying and Geospatial Eng., University of Tehran, Tehran, Iran.
E-mail addresses: hrasti@ut.ac.ir (H. Rastiveis), seydi.teymoor@ut.ac.ir (S. Teymoor Seydi), chenzhiq@umkc.edu (Z. Chen), junli@uwaterloo.ca (J. Li).

https://doi.org/10.1016/j.jag.2023.103450
Received 21 April 2023; Received in revised form 6 July 2023; Accepted 3 August 2023

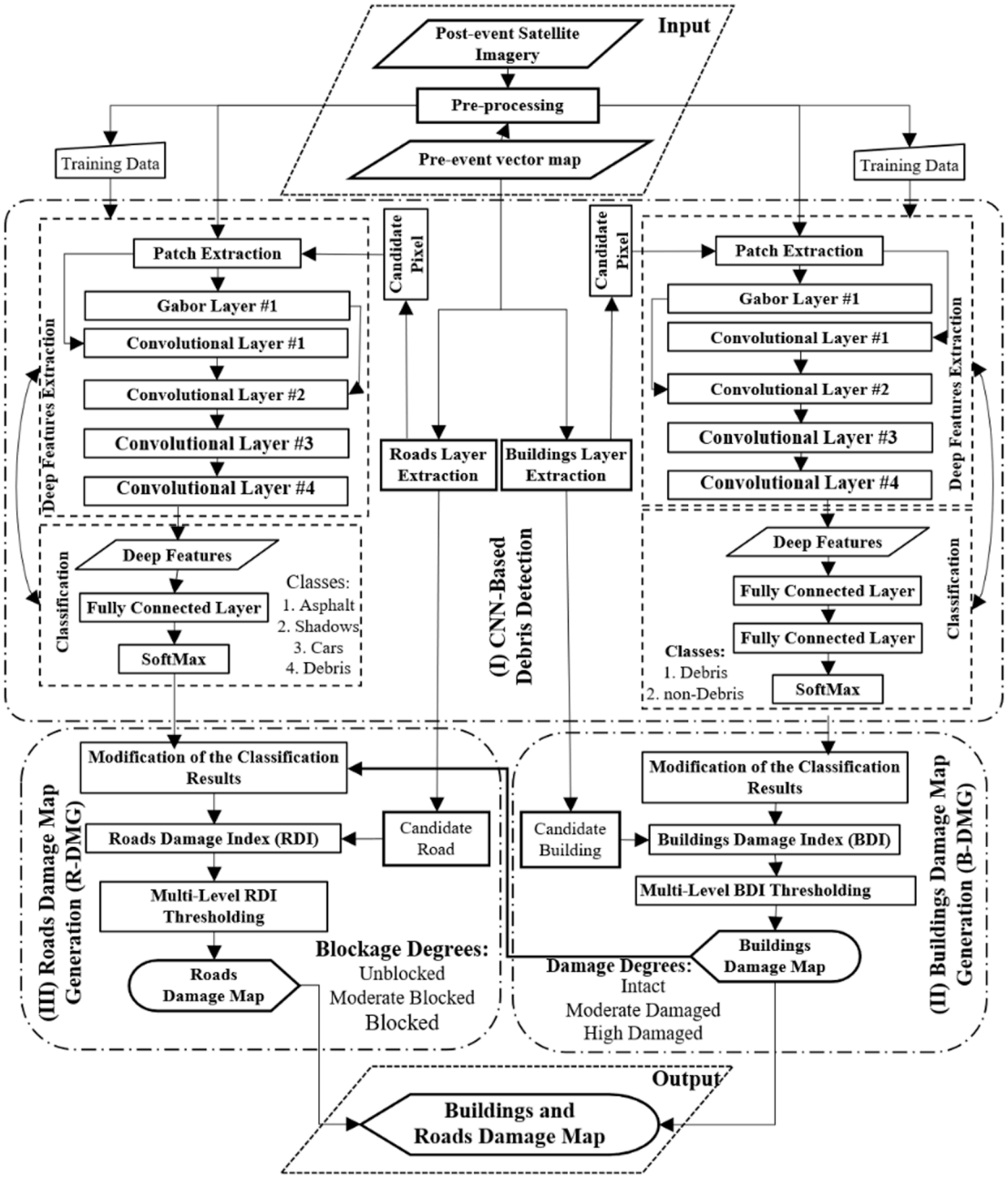

Fig. 1. The BR-DMG flowchart for earthquake-induced buildings and road damage map generation.

imagery to simultaneously generating both buildings and roads damage maps. The following section will review the previous traditional and DL-based methods for damage assessment.

1.2. Literature review

Previous damage detection methods have often relied on comparing pre- and post-event images using change detection methods (Menderes et al., 2015; Zhou et al., 2019). For instance, Erdogan and Yilmaz (2019) proposed a framework for building damage maps generation (B-DMG) using pre- and post-earthquake aerial photos and digital surface models (DSM). They employed an image differencing algorithm to identify change areas, and applied a threshold selection method to detect earthquake-induced changes.

Another common method for damage assessment is detecting debris areas on satellite images using classification techniques. Classification algorithms are typically employed for this purpose, with textural information being the most commonly used features for debris detection. In this regard, Haralick features, generated through grey level co-occurrence matrices (GLCM), have frequently been used for damage assessment (Samadzadegan et al., 2008). Khodaverdizahraee et al. (2020) proposed a state-of-the-art segment-by-segment comparison (SBSC) method based on object-oriented classification for B-DMG using satellite images. Their approach involved segmenting both images, performing a segmentation intersection to extract identical image objects, extracting optimal textural features for these objects, and utilizing the differences between pre- and post-event images in a support vector machine (SVM) classifier to detect damaged buildings. Cooner et al. (2016) evaluated building damages in three different scenarios including Artificial Neural Network (ANN), Radial Basis Function Neural Network (RBFNN), and Random Forest (RF), and reported an overall accuracy of 77%. Taskin Kaya et al. (2011) used the same dataset for

damage assessment based on support vector selection and adaption (SVSA), achieving an overall accuracy of 81%. While B-DMG methods using multi temporal optical remote sensing have shown acceptable results, they often face challenges due to the requirement of a pre-event dataset that may not always be available or up-to-date. Furthermore, collecting training data for classification twice can be a time-consuming process.

Surprisingly, there have been fewer studies focusing on road damage map generation (R-DMG) compared to B-DMG, despite the crucial role of road damage maps in post-earthquake search and rescue operations. However, several methods have utilized high-resolution optical imagery or LiDAR point clouds for R-DMG. For instance, Coulibaly et al. (2015) and Rastiveis et al. (2015) employed SVM classification for R-DMG using textural, spatial, and spectral features. Although R-DMG methods have demonstrated promising results, they often neglect the impact of building debris, and heavily rely on the availability of a pre-event image.

In recent years, several damage assessment techniques based on deep learning (DL) have been proposed. Nex et al. (2019) introduced a convolutional neural networks (CNN)-based architecture for identifying visible earthquake damages using optical sensors with different resolutions, generating a binary building damage map. Hao et al. (2018) proposed a combined 3-D convolutional neural network and Gabor filters (GNN) method for post-earthquake IKONOS image classification. Their proposed GNN model uses multi-scale spatial information scales by Gabor filters. Their GNN model outperformed SVM algorithm in classifying the image into four classes of Intact building, Forest, Broken Building, and Bareland. Yang et al. (2020) proposed a method for extracting road blockage information from post-earthquake high-resolution imagery using a low-depth CNN.

Most state-of-the-art DL-based damage assessment methods utilize deep architectures such as Fully Convolutional Networks (FCN), VGG, and U-Net (Ma et al., 2020; Shao et al., 2020) to extract deep features. While these architectures have demonstrated fascinating results, their effectiveness relies on a substantial amount of sample data, which can be a time-consuming and laborious process. Additionally, processing such complex networks requires powerful hardware. The complexity of these networks also makes it challenging to tune their hyperparameters and train them effectively.

In summary, generating a damage map based on change detection methods using bi-temporal imagery analysis is challenging because the changes can originate from other sources such as registration errors. In addition, it is a time-consuming and laborious process, which may not be a useful option for disaster managers to have a quick response after an earthquake. Although traditional methods based on textural information have reported promising results, selecting optimal features for classification is the main drawback of these methods. In the DL-based algorithms, this optimization is conducted by changing the weights between neurons in the last layer of the CNNs. It worths mentioning that regardless of promising results of the previous DL-based algorithms, their models possess complex network architecture and a very large number of model parameters. Hence, they demand high-volume training datasets, for which the process of preparing these semantically annotated datasets is tedious and demanding.

1.3. Contribution

Reviewing the previous methods on damage map generation using satellite imagery reveals potential for further improvement. This research proposes a deep learning-based method for creating a comprehensive urban damage map using satellite optical imagery. The proposed method introduces two CNNs to extract debris for buildings and roads. These CNNs, combined with a low-level feature extraction technique based on classical Gabor filters, offer a lower computational complexity compared to advanced deep learning frameworks. Consequently, the proposed CNN models are more efficient in training due to reduced network parameters, requiring a smaller training dataset.

A novel design aspect of the proposed method involves utilizing the produced building damage map as auxiliary data, along with the extracted debris areas on the road surface, to generate the road damage map. The visualization of features extracted from the shallow layers demonstrates their similarity to Gabor features. Gabor filters possess steerable properties that allow for the extraction of structures at specific frequencies and orientations from an image. These advantages have made Gabor filters popular tools in various image processing applications. By incorporating Gabor filters, the training complexity of the CNN is reduced, resulting in a decreased number of trainable parameters. Furthermore, the Gabor filter enhances the network's resistance to geometric transformations, thus improving the robustness of learned features against scale and rotation. This represents a key contribution of this paper—highlighting the potential benefits of Gabor filters in DL-based damage assessment.

In addition, this research introduces two new indices for measuring the level of damage to buildings and roads. Numerical studies and performance assessments using real earthquake event images are conducted to demonstrate and verify the proposed method. Notably, the proposed method only requires the post-event image for damage map generation. Furthermore, the algorithm can provide multi-level damage maps for roads and buildings, whereas many state-of-the-art methods focus on binary damage map generation. Another contribution of this paper is the reduction of false-positive debris pixels by establishing a connection between road debris and damaged buildings.

2. Method

Fig. 1 depicts the flowchart of our framework for urban buildings and road damage mapping (BR-DMG). The proposed framework is made up of three major components: (i) CNN-based debris detection to detect debris pixels on roads and buildings, (ii) B-DMG process to evaluate the damage degree of each building, and 3) R-DMG process to estimate the blockage level of the roads using the detected debris areas and the generated building damage map.

2.1. CNN-based architecture for debris detection

Because debris areas are a true indication of building damage or road blockage, debris detection constitutes the first step of the proposed BR-DMG method, implemented using CNN-based classification techniques. It is noteworthy that the variety of objects in the building area differs from the road surfaces; therefore, different CNN structures are used in each phase. To clarify, after an earthquake pixels of a building area in a satellite image can be categorized into two groups of Debris and non-Debris classes, and a binary classifier may satisfy this categorization. On the other hand, objects on the road surface are more diverse; here, Shadows, Cars, Asphalt, and Debris are five considered classes in roads area classification, which requires a more complex classifier.

The CNN has several layers connected sequentially by learnable weights and biases. These stacked convolutional kernels learn picture characteristics in spectral and texture space. CNN models for image classification usually have two primary parts: a feature extractor with multiple convolutional layers and an MLP classifier.

2.1.1. Gabor filter

The Gabor filter is a popular method of feature extraction that has been widely used in the field of image processing. This filter can be used directly, without any pre-processing, to extract features from grayscale images in a variety of scales and orientations. It involves a Gaussian function modulated by complex sinusoidal frequency and orientation. The general form of a 2D complex Gabor filter is defined by the following equation (Jia et al., 2021):

$$\mathscr{K}(x,y;\lambda,\alpha,\sigma,\varphi,\gamma) \equiv e^{-\frac{(z_1^2-\gamma^2 z_2^2)^2}{2\sigma_x^2}} e^{i(2\pi\frac{z_1^2}{\lambda}+\varphi)} \quad (1)$$

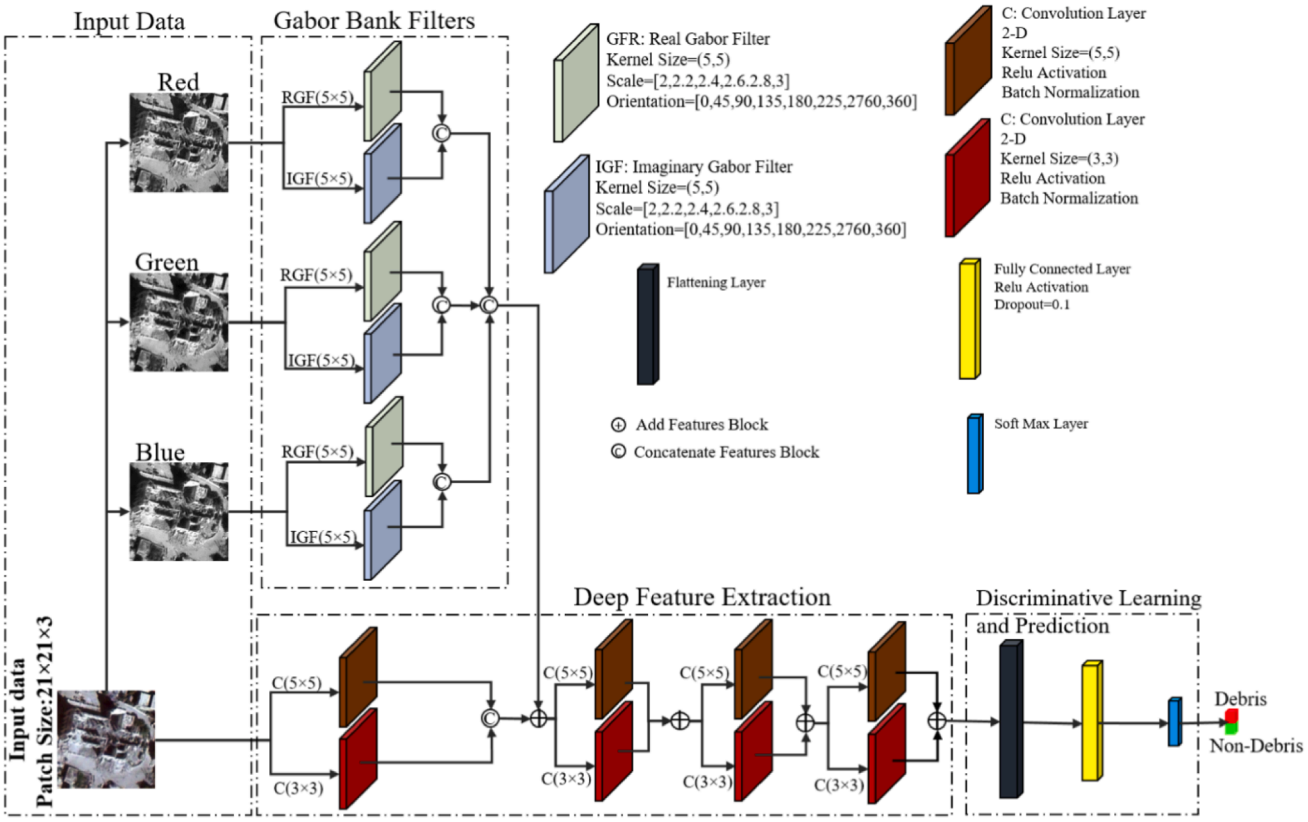

Fig. 2. The proposed CNN architecture for the B-DMG part.

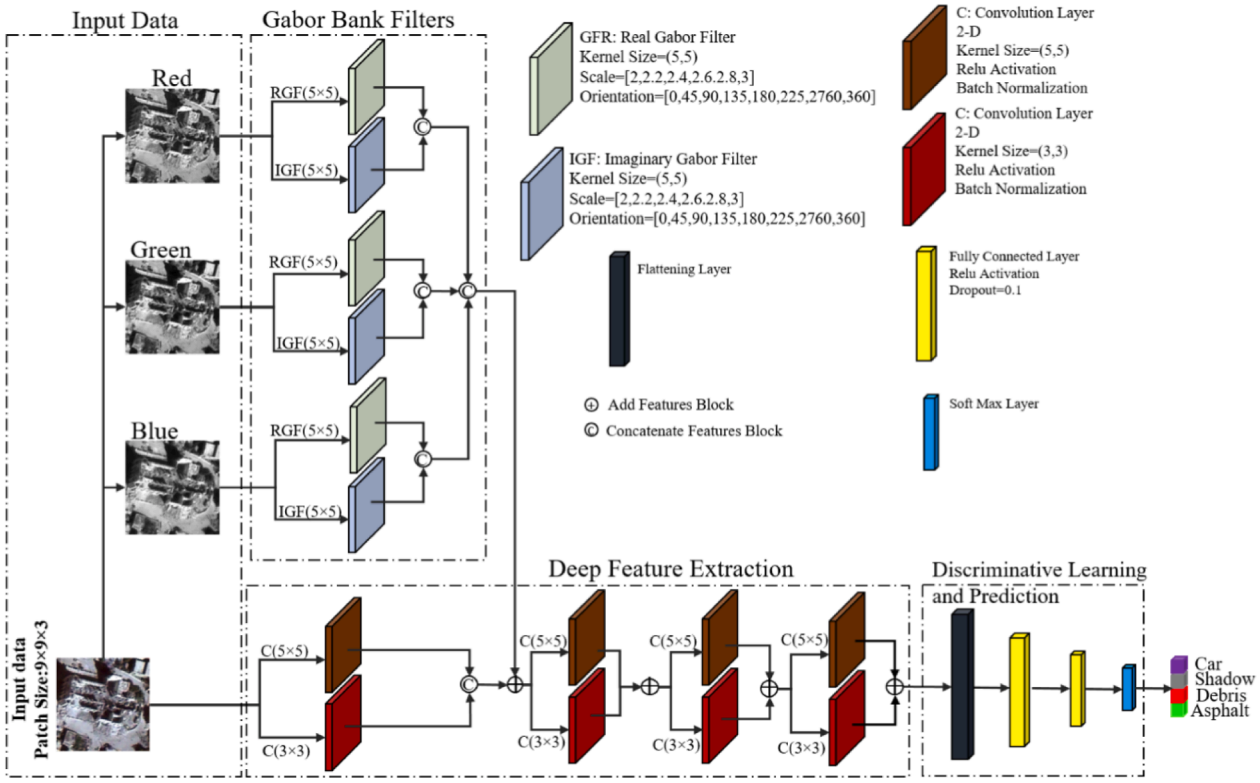

Fig. 3. The architecture of the CNN network for R-DMG purposes.

$$Z_1 = x\cos\alpha + y\sin\alpha \quad (2) \qquad Z_1 = -x\sin\alpha + y\cos\alpha \quad (3)$$

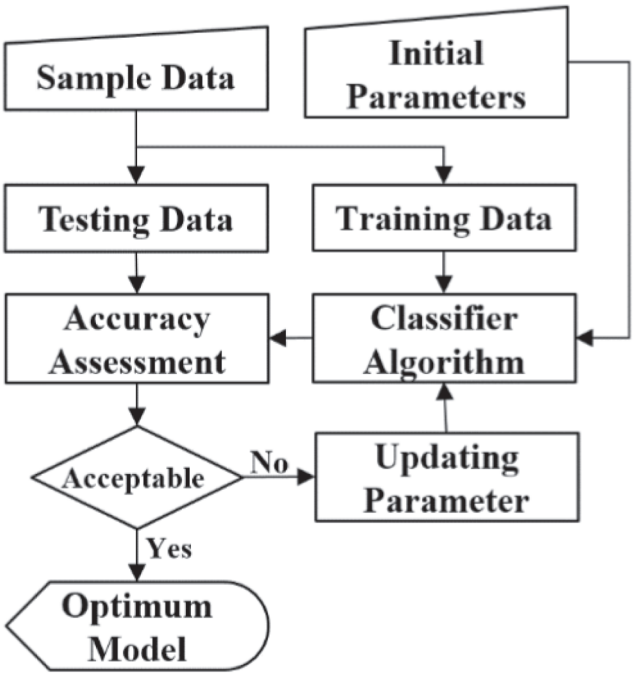

Fig. 4. The process of the supervised classification process.

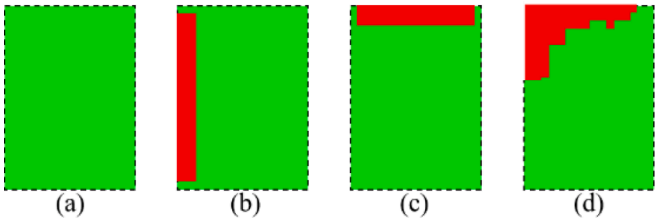

Fig. 5. The various distribution of debris inside a building; (a) building with no debris par; (b) destroyed along the width; (c) destroyed along the length; (d) destroyed in both length and width.

where x, y are pixel positions in the grey level image, σ standard deviation of the Gaussian function, λ wavelength of the sinusoidal plane wave, α is the orientation, γ is the spatial aspect ratio, and φ is phase offset,

The real part of a 2D Gabor Filter ($\mathscr{H}_r$) can be defined as follows:

$$\mathscr{H}_r(x,y;\lambda,\alpha,\sigma,\varphi,\gamma) \equiv e^{-\frac{(Z_1^2-\gamma^2 Z_2^2)^2}{2\sigma_x^2}} \cos(2\pi\frac{Z_1^2}{\lambda}+\varphi) \tag{4}$$

The 2D Gabor Filter's imaginary component ($\mathscr{H}_i$) can be described as:

$$\mathscr{H}_i(x,y;\lambda,\alpha,\sigma,\varphi,\gamma) \equiv e^{-\frac{(Z_1^2-\gamma^2 Z_2^2)^2}{2\sigma_x^2}} \sin(2\pi\frac{Z_1^2}{\lambda}+\varphi) \tag{5}$$

The 2D Gabor Filter's real and imaginary components are applied to the greyscale image at various angles and sizes. The output of Gabor Filter is fused with the first layer of CNN and fed to the next layers to generate high-level features.

2.1.2. Convolution layer

The convolution layer automatically extracts deep features by a combination of linear and non-linear operations based on the following equation (Barzegar et al., 2023):

$$v_{i,j} = f\left(\sum_{s=1}^{q}\sum_{t=1}^{q} w_{s,t}.v_{i+s,j+t} + b\right) \tag{6}$$

where f denotes the activation function, W is the convolution filter with a size of $q \times q$, v is the feature map at the preceding layer, b is the bias, and (.) is the dot product operator. The output of the j^{th} feature map in the i^{th} layer at (x,y) can be expressed using the following equation (Saadat et al., 2022):

$$v_{i,j}^{xy} = f\left(b_{i,j} + \sum_{m}\sum_{r=0}^{L_i-1}\sum_{s=0}^{Q_i-1} W_{i,j,m}^{r,s} v_{i-1,m}^{(x+r)(y+s)}\right) \tag{7}$$

where L and Q are the length and width of the convolution filter size, respectively, and m is the feature related to the current feature in the $(i-1)^{th}$ layer.

2.1.3. Architectures

Due to the diversity of the objects on the road area against the simplicity of the building area, different CNN architectures are considered. The CNN architecture for buildings should divide the building area into two classes "Debris" and "non-Debris". Fig. 2 depicts the architecture of the suggested CNN model for B-DMG, which consists of an input layer, an extraction layer using a Gabor bank filter, four convolution layers, and a fully connected layer. The size of the input patch in this network is 21 × 21 pixels. The number of kernels and their size in the convolutional layer are depicted in Fig. 2. The extracted deep features are incorporated into a fully connected (FC) layer, and then a softmax is used to determine the classification of the input patch with probabilistic values between 0 and 1. It should be noted that unlike the GNN model, proposed by Hao et al. (2018), our proposed model extract gabor features for each channels of the image separately and use the resulted gabor features along with the original image as the input of the convolutional layers.

In the road area, various classes such as cars, debris, asphalt, and shadows exist; therefore, detecting debris areas on the road surface requires a more complex CNN architecture compared to the B-DMG's architecture. For this purpose, an extra fully connected layer is considered in addition to the higher number of filters in the convolutional layers. The designed architecture for R-DMG is illustrated in Fig. 3.

2.2. Model training and prediction

Fig. 4 illustrates the general overview of the training process. As shown in this figure, the optimization of the parameters is performed in two iterative steps: (i) learning the classifier algorithm based on training data and initial parameters, and (ii) evaluating the classifier using test data. These steps are repeated until reaching an acceptable accuracy.

Our proposed CNN models utilize back-propagation for supervised learning techniques in their training process. The main idea is to adjust the weights in the nodes to minimise the difference between the output node activation and the output (Zhang et al., 2019). By back-propagating the errors through the network, the weights are adjusted using a recursive method. This process will continue until the error become lower than a predefined acceptable value.

The quality and quantity of sample data are crucial to the efficacy of supervised machine learning systems. As can be seen from Fig. 5, the sample data is divided into two main parts: (1) training data, and (2) testing data. The training data is divided into training and validation data, which are used for training and validating the data while tuning the parameters of the models.

In this study, to train the CNNs, several sample data in two classes of Debris and non-Debris were manually collected to be used for training the proposed CNN in the B-DMG module. In the R-DMG module, the selected sample data were collected in four classes Asphalt, Debris, Cars, and Shadows. Eventually, using the abovementioned CNNs the debris

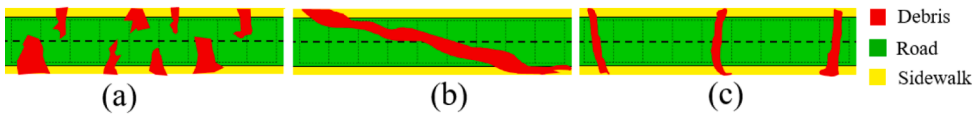

Fig. 6. Various distributions of debris on a road surface; a) high amount of debris in an unblocked road; b) sample of debris distribution that may not be accurate by road sectioning or profiling; c) low amount of debris area in a blocked road.

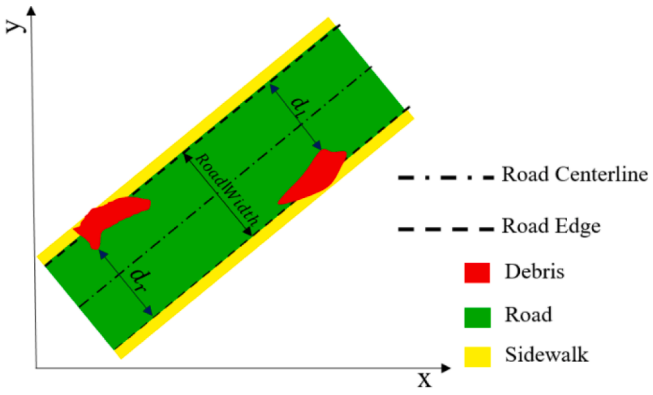

Fig. 7. Schematic diagram of damaged road consideration based on RDI.

pixels are detected in both roads and buildings area. These pixels are then used for evaluating the level of damage in the next steps.

2.3. Damage map generation

2.3.1. Building damage map generation

The extracted debris of each building is used to detect the level of damage to that building. It should be noted that small objects on the roof of some buildings such as solar panels, air conditioners, and TV antennas may cause false alarms in the classification step. Therefore, in a modification step of the B-DMG, a closing morphological operator is used to eliminate the noisy debris areas considering a square-shaped structural element with a 3 pixels width. Here, the shape and size of the structural element must be selected carefully to not eliminate large debris parts. After the modification, all buildings with no debris areas are labeled as "Intact buildings" while the others are evaluated via a damage analysis process.

There are various criteria for damage analysis that mainly focus on the geometrical properties of the debris parts including length, width, and area. Defining the damage index merely based on one of these parameters may lead to an incorrect damage degree. This is clarified by the presented samples in Fig. 5 which debris parts may appear in any direction in any area.

In this research, therefore, all of these three geometrical parameters are used to calculate a building damage index (BDI). For this purpose, three initial damage indexes based on each of these parameters (i.e. area (DI_A), width (DI_W), and length (DI_L)) are measured using Eqs. (8)–(10), and then the average of these indices is used to define the final building damage index (BDI) as shown by Eq. (11).

$$DI_A = \frac{\text{Area of the Debris}}{\text{Area of the Building}} \tag{8}$$

$$DI_W = \frac{\text{Width of the Debris}}{\text{Width of the Building}} \tag{9}$$

$$DI_L = \frac{\text{Length of the Debris}}{\text{Length of the Building}} \tag{10}$$

$$BDI = \frac{DI_A + DI_W + DI_L}{3} \tag{11}$$

Once the BDI is calculated for all buildings in the damaged area, some predefined thresholds on the BDI map can be utilized to provide a multi-level building damage map. The bigger BDI value indicates more similarity between the debris area and the initial building polygon which is a sign of a highly damaged building. Conversely, if the BDI is small, which is a sign of a small and narrow debris area, then the building would be labeled as low-level damage. The minimum and maximum value of the BDI is 0 and 1, respectively. Dividing this interval, the final damage map is obtained in three levels of damages: intact or low-level damaged building, moderate-level, and high-level damage degrees.

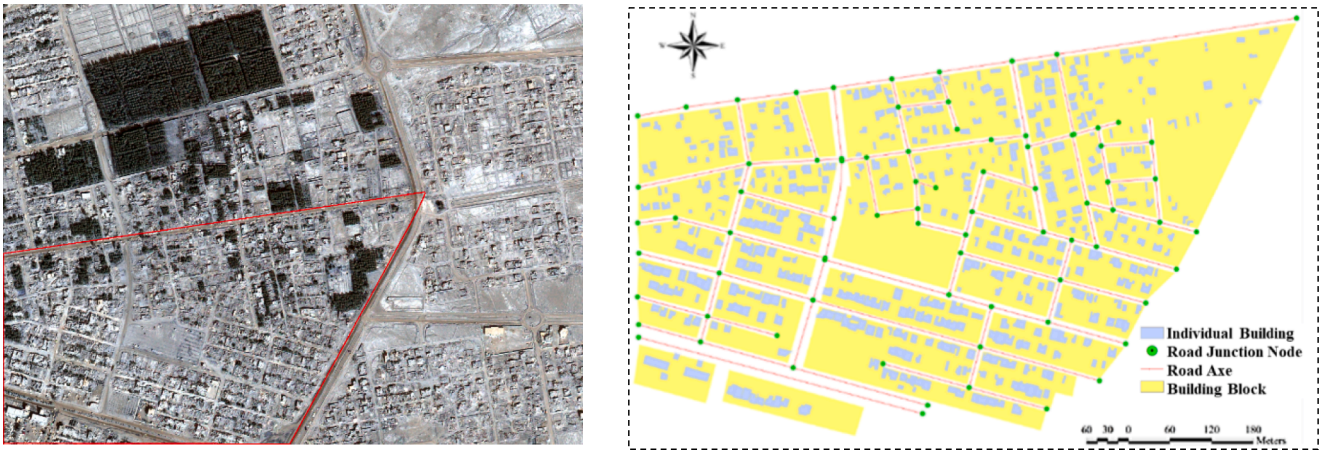

Fig. 8. Overview of the Bam dataset as the first dataset in this research; a) Post-earthquake high-resolution data that the selected test area is bolded by the red polygon; b) The pre-event vector map of the selected test area. (For interpretation of the references to color in this figure legend, the reader is referred to the web version of this article.)

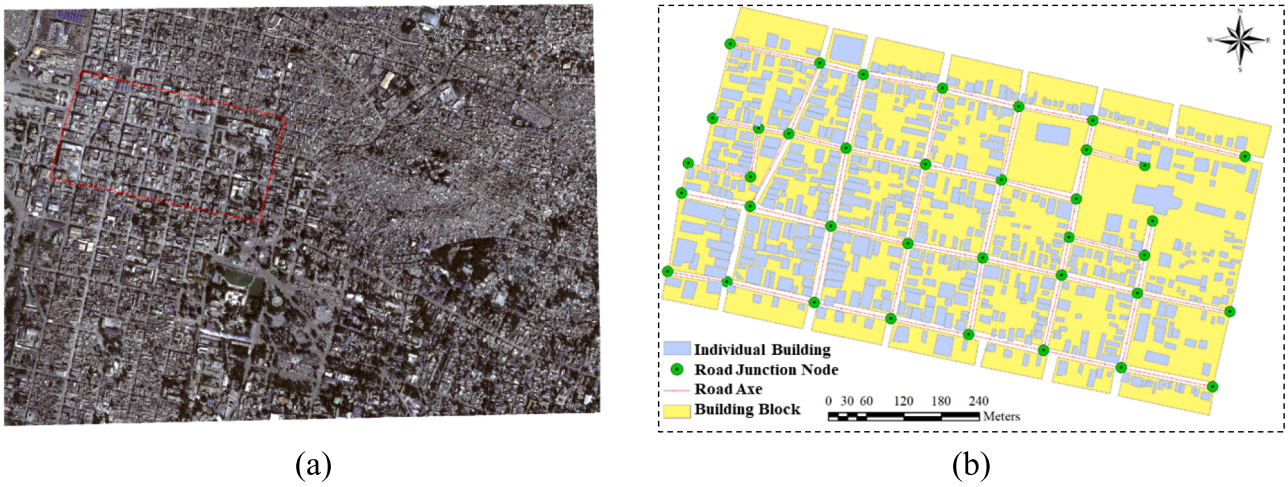

Fig. 9. Haiti dataset: (a) Post-earthquake WorldView-2 image; (b) obtained layer of the road network from the open street map overlaid on the resulted building polygons from the pre-event image interpretation.

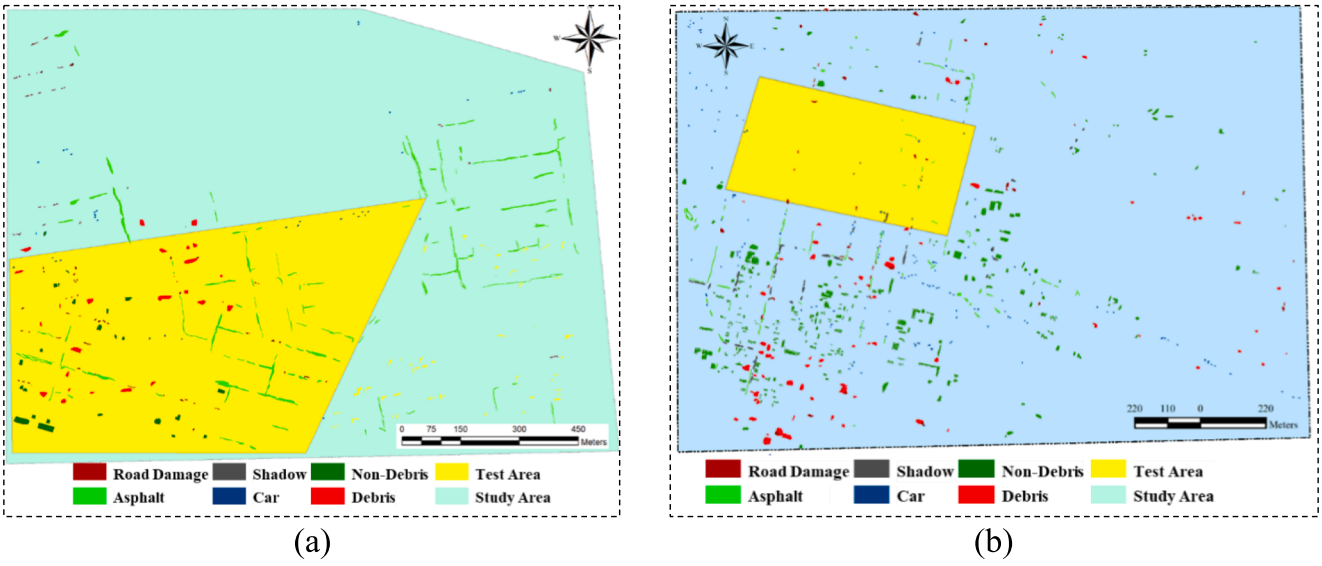

Fig. 10. Spatial distribution of the selected samples to train the proposed models for classification: (a) Bam dataset; (b) Haiti dataset.

Table 1
Numbers of samples used for damage detection in the Bam dataset ().

	No. of Pixels in the Test Area	Class	No. of Samples	Training	Validation	Testing
B-DMG	486,503	*Non-Debris*	7505	4803	1201	1501
		Debris	8440	5401	1351	1688
R-DMG	241,689	*Car*	942	602	152	188
		Asphalt	27,374	17,519	4380	5475
		Shadow	5218	3339	835	1044
		Debris	2057	1316	328	411

*Unit of samples is pixel.

2.3.2. Road damage map generation

Similar to the B-DMG, the R-DMG process starts with modification of the classification result followed by a road damage index (RDI) calculation to evaluate the blockage level for each road segment. The main purpose of the modification process in this module is to detect and eliminate false debris areas inside the road area. If we assume that all debris areas inside a road originate from building damages, we can eliminate false debris areas by considering the resulted building damage map. In other words, a debris area on the road will be accepted if there is at least one damaged building near that debris area. Here, after eliminating noisy debris pixels using a morphological operator by using a square-shaped structural element with a 3 pixels width, another modification is used based on the generated building damage map. In which, a buffer space perpendicular to the road direction is considered for each debris part to detect all adjacent buildings to that debris part. Due to the assumption that building debris is the main reason for a road blockage after an earthquake, not observing a damaged building inside the buffer space can be a sign of classification errors, and consequently, that debris

Table 2
Numbers of samples used for damage detection in the Haiti dataset.

	No. of Pixels in the Test Area	Class	No. of Samples	Training	Validation	Testing
B-DMG	194,406	*Non-Debris*	19,763	12,648	3162	3953
		Debris	10,192	6523	1631	2038
R-DMG	274,767	*Car*	5229	3347	837	1045
		Asphalt	8968	5739	1435	1794
		Shadow	4505	2883	721	901
		Debris	8088	5176	1294	1618

*Unit of samples is pixel.

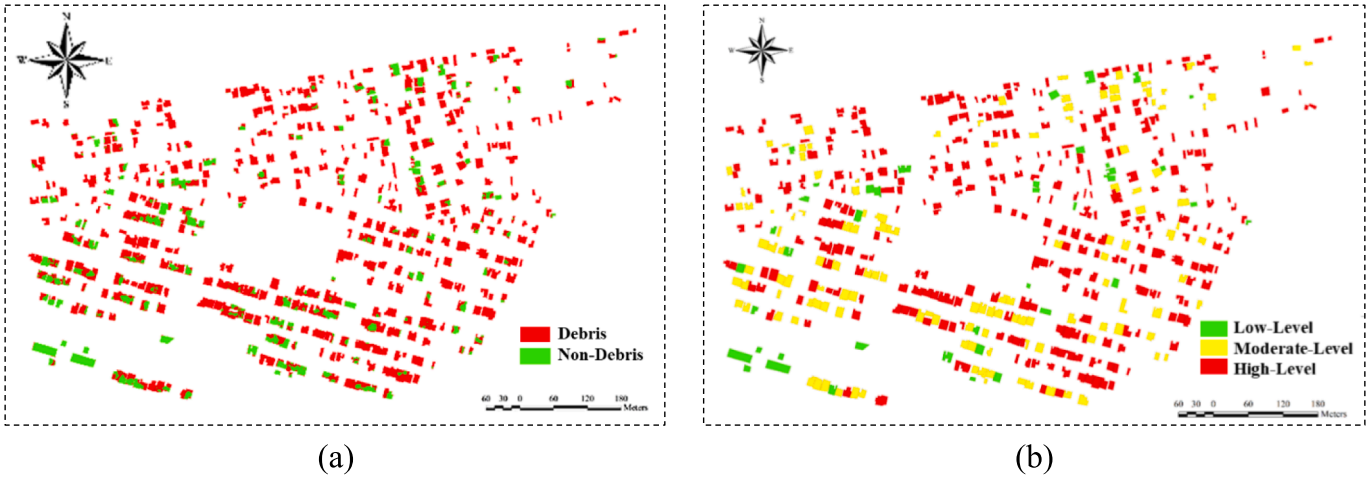

Fig. 11. Results of the B-DMG module in Bam dataset: (a) classified buildings using the proposed CNN in two classes; (b) building damage map showing three levels of building damages.

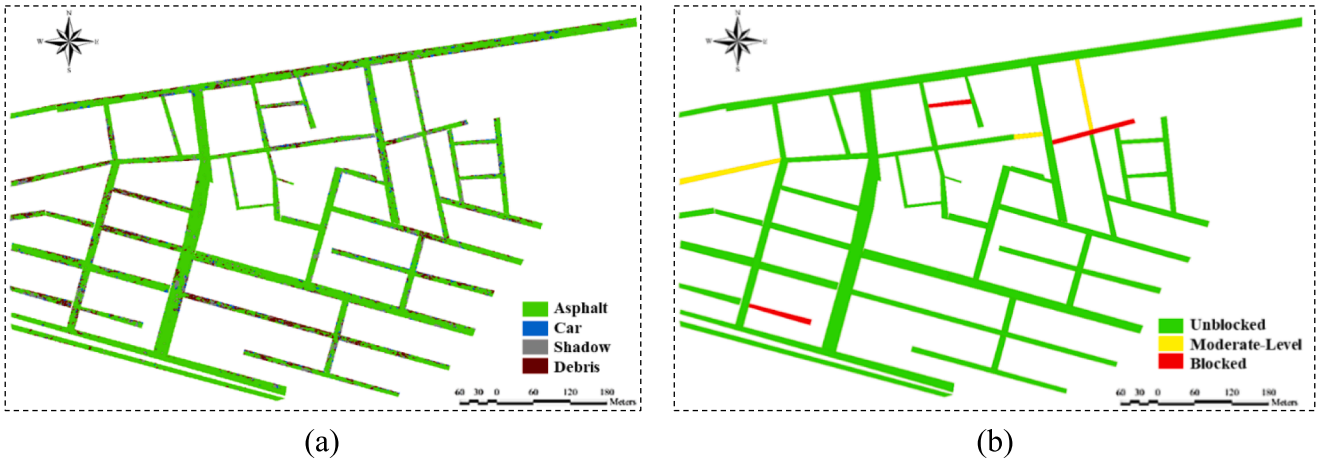

Fig. 12. Results of the R-DMG module in the Bam dataset: (a) classified roads using the proposed CNN in four classes; (b) road damage map with three levels of road damages.

area can be eliminated from the road segment.

Once the classification results are modified, the blockage level of each road can be assigned based on the extracted debris areas. Surely, the amount of debris inside a road is not an accurate index for evaluating the road's blockage but its distribution form is significant. Fig. 6 illustrates three different possible cases of debris distribution. For example, Fig. 6a shows an unblocked road with a large amount of debris on the road surface while Fig. 6c shows a blocked road with a small and narrow debris area. Several previous studies have used road profiling or sectioning for their damage analysis in which a road is divided into several tiles or sections, and the blockage of these sections is considered to make the final decision about the road situation (Izadi et al., 2017; Samadzadegan and Zarrinpanjeh, 2008). Although these methods may provide promising results, however, they may not be accurate in some cases. For instance, in Fig. 6b there is an inclined debris area that has blocked the road. If one divides this road into many segments, all segments in this road may appear unblocked, and consequently, it would be labeled an unblocked road while it is truly blocked.

In this study, the road damage index (RDI) is defined based on the orthogonal distance of the debris areas to the edge of the road. If this distance is larger than a standard parking width (e.g. 3 m), it means that the debris area has not completely blocked the road. As can be seen from Fig. 7, the orthogonal distance of each debris area to the road edges can be a useful sign of the openness of the road. It is worth mentioning that

Fig. 13. Final damage map of the test area for the Bam dataset using the proposed BR-DMG process with the three levels of damages.

small areas of sidewalks from both sides of the road are eliminated to measure the RDI in a more reasonable area. These areas, which are shown by the yellow color in Figs. 6 and 7, can be a fixed value or can be considered as a small percentage of the road width. In this research, we considered 2 m road width as the sidewalk buffer. Eventually, the road damage index for each debris part (RDI_i) is calculated using Eq. (12), and the final RDI for the road can be obtained using Eq. (13):

$$RDI_i = max\{d_{li}, d_{ri}\} \tag{12}$$

$$RDI = \min\{RDI_i\},\ i = 1, 2, \cdots, n \tag{13}$$

where n is the number of debris areas inside the road. d_{ri} and d_{li} are the distance of the i-th debris area to the right- and left side of the road, respectively. The higher value of these distances will show the low influence of the debris on the road blockage. The final RDI of the road is calculated based on the smallest RDIi among all debris areas. Similar to multiple damage map generation of buildings, predefined thresholds on the RDI measure can be used in the final road damage map.

3. Experiments and results

3.1. Datasets

The first dataset includes the pre-event digital vector map and post-event QuickBird satellite image of the city of Bam, Iran, taken on January 3, 2004, a week after the 2003 earthquake. The spatial resolution of this dataset is 2.4 (m) visible spectral bands and 0.6 (m) for panchromatic band. Also, The Intensity-Hue-Saturation (IHS) pan-sharpening technique was utilized to enhance the spatial resolution. The selected test area region of the Bam dataset can be seen within the red polygon in Fig. 8a.

The post-earthquake WorldView-2 image of Port-au-Prince, Haiti is used as the second dataset to evaluate the proposed CNN-based BR-DMG method. The WorldView-2 image was acquired on January 13th, 2010, with spatial resolutions of 2 m and 0.5 m for multispectral and panchromatic bands, respectively. In this dataset, a region including several buildings was selected as the test area which is specified by a red polygon in Fig. 9a.

3.2. Model training process

The spatial distribution of the generated sample data for the Bam and Haiti datasets is presented in Fig. 10. The training, validation, and test data percentages in both networks were 64%, 16%, and 20%, respectively. More details of the selected samples are summarized in Tables 1 and 2 for both datasets.

The CNN hyper-parameters were also initialized and, then, examined on the testing data. The input patch size for B-DMG and R-DMG were 21 × 21 × 3 and 9 × 9 × 3, respectively. In addition, the size of the mini-batch was 1500. Moreover, the initial learning rate was set to 10^{-4} with an epsilon value of 10^{-9}. The dropout is a key parameter to avoid overfitting that was set to 0.1 rates in the latest layer.

3.3. Results

After pre-processing, by overlaying the buildings and road layers on the post-event image all buildings and road areas were extracted. It is noteworthy that the obtained areas merely help us to know which pixel should be imported into which classification process, and input patches to the network are selected from the original pre-processed image. This will help the network to have a fair and realistic view of the pixels located on the edges of the buildings or roads. Finally, the label of every candidate pixel inside the buildings or roads was predicted using their corresponding trained CNN model.

Fig. 11a shows the result of the building damage classification for the Bam dataset. Eventually, the final buildings damage map was obtained by thresholding the BDI measure that can be seen in Fig. 11-b. In this paper, those buildings whose BDI is less than 0.3 are labeled as *Intact* or *low-level damaged* buildings, those with BDI values between 0.3 and 0.5 as *moderate-damaged* buildings, and the buildings with BDI greater than

Fig. 14. Damage maps for the test area in Haiti dataset: (a) classified building area; (b) building damage map; (c) classified road area after modification; (d) road damage map with three levels of damages; (e) final damage map generated using the proposed BR-DMG process.

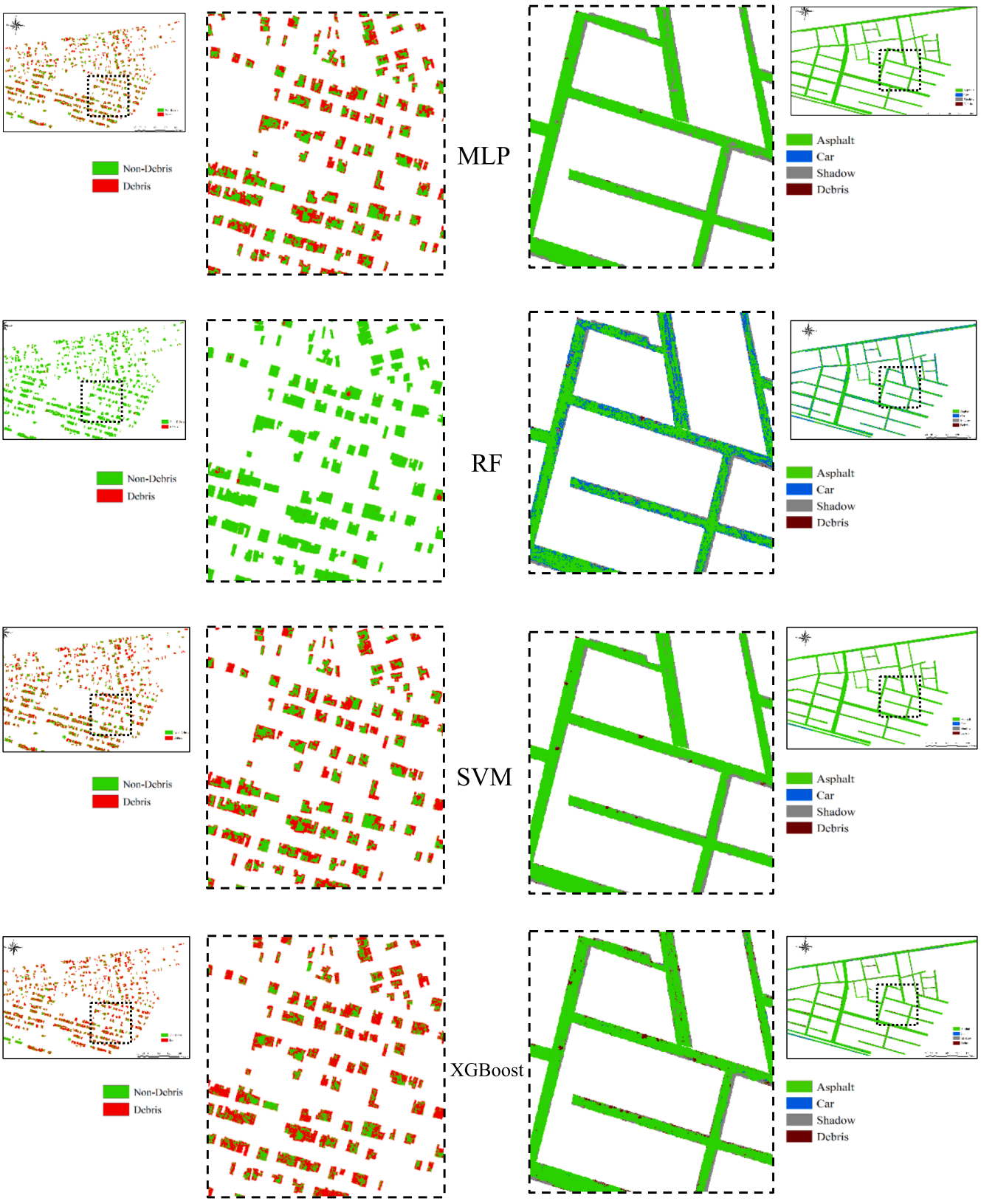

Fig. 15. Result of the conventional classification methods using Haralick texture features for B-DMG (left) and R-DMG (right) in the Bam dataset.

0.5 as *high-damaged* buildings. The multiple damage analysis for the buildings shows that a considerable number of buildings have been classified in the high-level damage class.

In the R-DMG module, the obtained classification result of the road regions using the proposed CNN model was modified using the resulted buildings damage map, and all false debris areas were eliminated from the result. Then, buffering 0.05% of the road width from each side, the RDI measure of all the road segments was calculated for evaluating the blockage degree. In this research, three degrees of blockage including *Unblocked*, *Moderate-level blocked*, and *Blocked* were considered. The

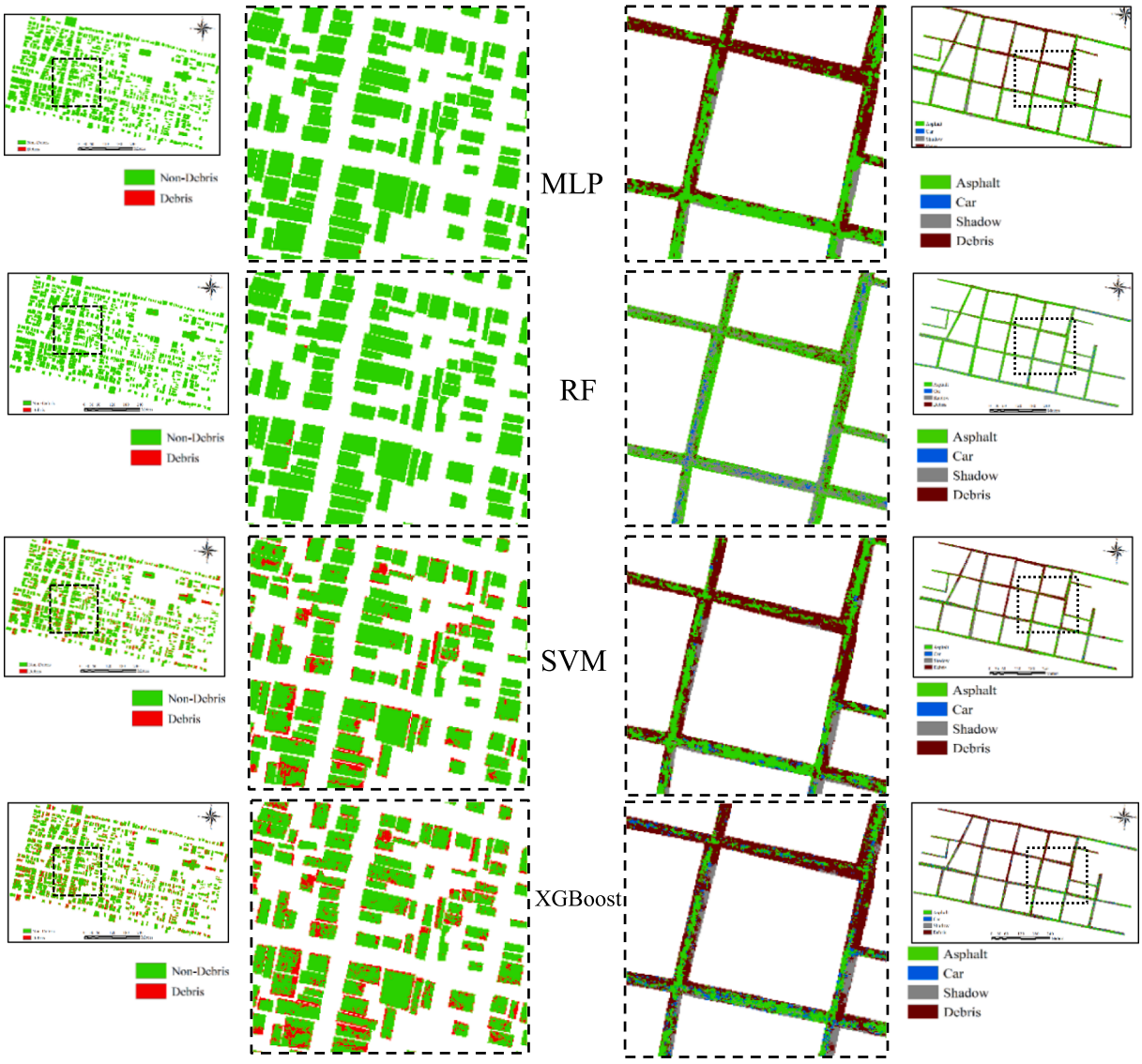

Fig. 16. Results of the conventional classification methods using Haralick texture features for B-DMG (left) and R-DMG (right) in the Haiti dataset.

Table 3
B-DMG module CNN-based classifier numerical assessment summary (UA: User Accuracy, PA: Producer Accuracy, OA: Overall Accuracy).

		Bam Dataset		Haiti Dataset	
		UA (%)	PA (%)	UA (%)	PA (%)
Non-Debris	MLP	63.66	71.55	66.59	100
	RF	77.41	73.75	75.32	88.46
	SVM	68.33	71.15	75.03	88.92
	XGboost	77.34	75.48	75.34	88.57
	Ours	**99.70**	**99.67**	**95.94**	**95.72**
Debris	MLP	71.57	63.68	100	2.70
	RF	77.6	80.86	66.17	43.77
	SVM	73.37	70.68	66.46	42.59
	XGboost	78.65	80.33	66.37	43.77
	Ours	**91.57**	**99.76**	**91.74**	**92.15**
OA (%)	MLP	67.39		66.90	
	RF	77.52		73.26	
	SVM	70.90		73.16	
	XGboost	78.05		73.33	
	Ours	**95.01**		**94.50**	

thresholds here are regarded as follows: roads whose RDI is smaller than 3 m are assigned as *Blocked* roads, from 3 m to 7 m as *Moderate-level Blocked*, and greater than 7 m are labeled as *Unblocked* roads. The classification image of the roads area for the Bam dataset after modification and the obtained roads damage map is shown in Fig. 12a and 12b, respectively.

Fig. 13 shows the final damage map after merging both the building damage map and the road damage map obtained using our proposed BR-DMG process for the Bam dataset.

Similarly, the damage map for the Haiti dataset was achieved. The detailed results including the classification results and the damage map of the B-DMG and R-DMG modules in addition to the final damage map are shown in Fig. 14.

3.4. Performance of the CNN classifiers

This section presents a comparison study between the designed CNN-based classification method (i.e., a CNN feature extractor plus an MLP classifier) and the four traditional ML methods (MLP, SVM, RF, and XGBoost classification models). In these methods, the Haralick textural features were extracted and used as suitable descriptors as they have been used in several damage assessment studies. It should be noted that

Table 4
R-DMG module CNN-based classifier numerical evaluation.

		Bam Dataset		Haiti Dataset	
		UA (%)	PA (%)	UA (%)	PA (%)
Asphalt	MLP	88.64	98.61	45.61	85.23
	RF	93.76	85.57	77.83	27.98
	SVM	88.72	99.27	50.48	79.10
	XGboost	90.45	98.10	58.32	72.30
	Ours	**98.79**	**98.65**	**98.59**	**93.53**
Car	MLP	0	0.00	72.41	2.01
	RF	7.74	41.49	27.34	55.02
	SVM	72.73	4.26	45.79	8.33
	XGboost	58.70	14.36	44.64	23.92
	Ours	**78.00**	**82.98**	**96.93**	**99.71**
Shadow	MLP	82.29	79.21	78.17	44.51
	RF	79.49	80.17	28.81	68.59
	SVM	90.13	77.01	66.91	51.83
	XGboost	89.75	81.32	66.44	55.38
	Ours	**93.40**	**93.49**	**99.76**	**94.01**
Debris	MLP	77.27	4.14	64.14	58.03
	RF	81.67	11.92	90.11	25.90
	SVM	75.28	16.30	59.98	61.50
	XGboost	64.36	29.44	61.55	69.34
	Ours	**78.82**	**77.86**	**90.53**	**96.91**
OA (%)	MLP	87.71		53.94	
	RF	79.36		39.46	
	SVM	88.70		55.39	
	XGboost	89.46		59.13	
	Ours	**96.28**		**95.84**	

in this paper we do not describe the details of the Haralick feature extraction. Interested readers are referred to (Löfstedt et al., 2019) for more details. During the ML classification, 8 Haralick features, which are the most used features in damage assessment studies, were selected. Regarding the parameter setting of these classifiers, the optimum value of the penalty coefficient (C) parameter and the kernel parameter (γ), in SVM were considered 34.29 and 0.001, respectively. In the MLP classifier, 3 hidden layers were considered, and cross-entropy was used as the network performance function. This MLP classifier was converged after 100 iterations. The RF classifier parameters had set as follows: Number of Trees = 105, Number of Features to Split Each Node = 3. In addition, the XGboost classifier parameters had set as: Nrounds = 305, Max-Depth = 5, Eta = 0.03, Gamma = 0, Min-Child-Weight = 1, Subsample = 0.8, Colsample-Bytree = 0.8.

The results of using the MLP, RF, SVM, and XGboost methods are shown in Figs. 15 and 16 for the Bam and Haiti datasets, respectively. As shown in Figs. 15 and 16 the obtained results from these two classifiers based on texture features are noisy and irrational and include too many false pixels while the classified image obtained by the CNN, shown in Fig. 12a, is more logical. The RF classifier is more sensitive to the detection of Non-Debris while it had missed its performance in the detection of Debris pixels. Furthermore, the other classifiers had provided noisy pixels in the detection of Debris pixels.

To evaluate the performance of the proposed CNNs for debris detection in B-DMG and R-DMG modules, quantitatively, common numerical measures including overall, user, and producer accuracies were calculated and compared with the result of the traditional machine learning algorithms. The obtained accuracy parameters are summarized

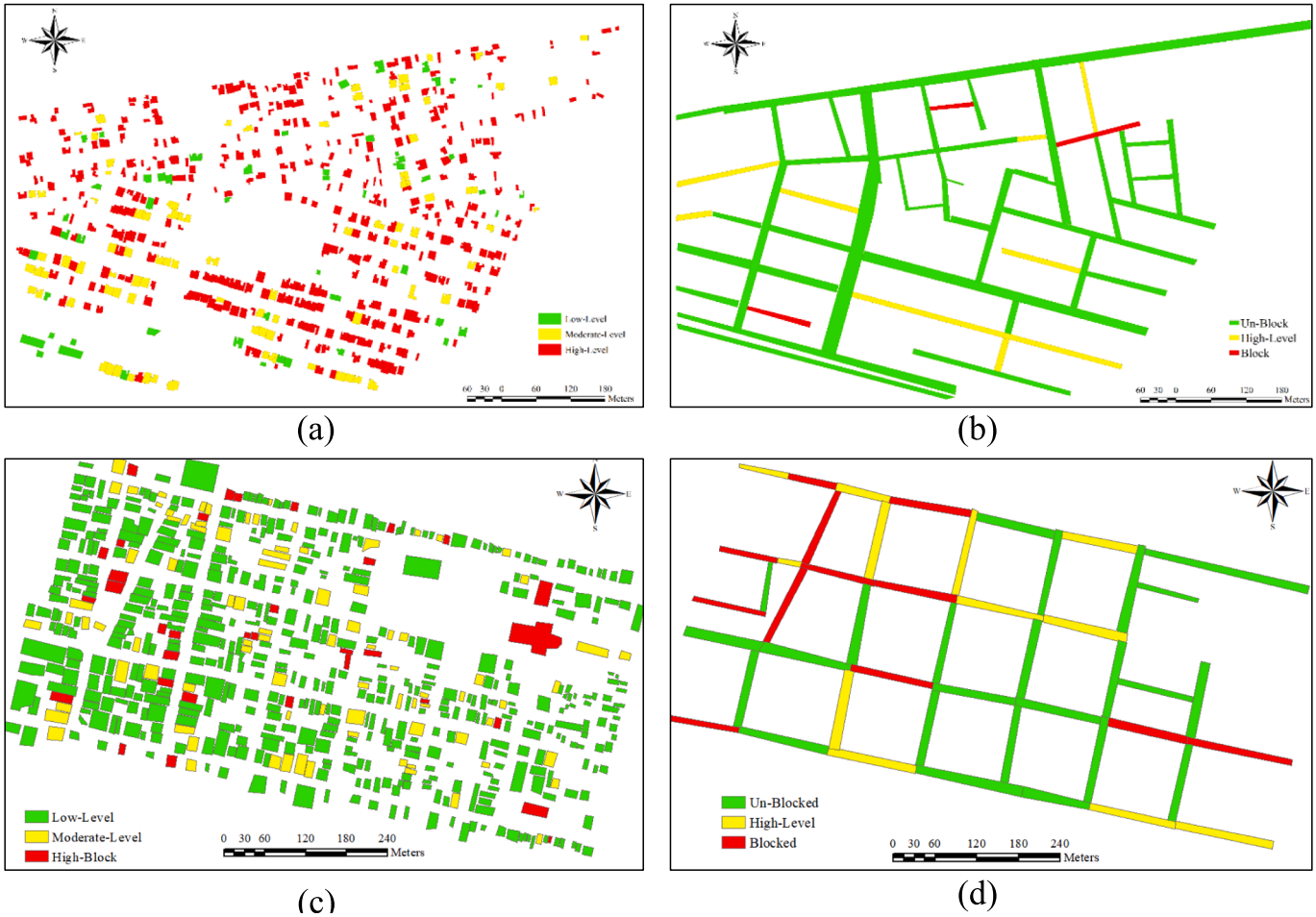

Fig. 17. Visually evaluated buildings and roads for accuracy assessment. (a) and (b) buildings and roads of the Bam dataset; (c) and (d) buildings and roads in the Haiti dataset.

Table 5
The accuracy of the obtained building and road damage maps is evaluated by comparing them to the reference maps of both datasets (IB: Intact-Building; MLD: Moderate-Level Damage; HLD: High-Level Damage; U: Unblocked; B: Blocked; MB: Moderate Blocked; CO: Classification Overall; TO: Truth Overall).

	Bam Dataset						Haiti Dataset					
Buildings Damage Map	**UA (%)**	**CO**	**HLD**	**MLD**	**IB**		**IB**	**MLD**	**HLD**	**CO**	**UA (%)**	**Buildings Damage Map**
	88.46	26	0	3	23	**IB**	537	16	5	558	96.23	
	57.24	138	49	79	10	**MLD**	33	79	5	117	67.52	
	94.30	351	331	14	6	**HLD**	1	3	31	35	88.57	
	—	515	380	96	39	**TO**	571	98	41	710	—	
	—	—	87.10	82.29	58.97	**PA (%)**	94.05	80.61	75.61	—	—	
	84.08					**OA (%)**	91.13					
	UA (%)	**CO**	**B**	**MB**	**U**		**U**	**MB**	**B**	**CO**	**UA (%)**	
Roads Damage Map	92.06	63	0	5	58	**U**	23	3	0	26	88.46	**Roads Damage Map**
	100	3	0	3	0	**MB**	0	9	2	11	81.81	
	100	3	3	0	0	**B**	1	0	10	11	90.91	
	—	69	3	8	58	**TO**	24	12	12	48	—	
	——	—	100	37.5	100	**PA (%)**	95.83	75.00	83.33	—	——	
	92.75					**OA (%)**	87.50					
	Bam Dataset						**Haiti Dataset**					

Table 6
Comparison of high-resolution satellite image debris detection techniques.

	Reference	Method	OA (%)
Buildings Damage Map Generation (B-DMG)	Taskin Kaya et al. (2011)	Support Vector Selection and Adaption (SVSA)	81
	Cooner et al. (2016)	#1: Artificial Neural Network (ANN)	74
		#2: Radial Basis Function Neural Network (RBFNN)	77
		#3: Random Forest (RF)	76
	Bai et al. (2018)	Object-based classification	91
	Mangalathu and Burton (2019)	Deep Learning-based (LSTM)	86
	Hao et al. (2018)	3-D Gabor Convolutional Neural Network	71
	Ours	Deep Learning-based (CNN)	93
Roads Damage Map Generation (R-DMG)	Wang et al. (2015)	Knowledge-based Detection	85
	Rastiveis et al. (2015)	support vector machine (SVM)	83
	Ours	Deep Learning-based (CNN)	87

in Tables 3 and 4 for the B-DMG and R-DMG, respectively. Based on the numerical results presented in these tables (Tables 3, 4), the CNN classifiers outperformed the other methods in both modules. Additionally, the performance of the model in R-DMG is better than in B-DMG for both datasets.

3.5. Accuracy assessment of the damage maps

The obtained damage maps from the algorithm are compared with the manually extracted damage maps based on visual interpretation of the pre- and post-earthquake images to assess the reliability of our method. Comparing these visually obtained damage maps, as shown in Fig. 17 for both datasets, with the results of the algorithm, the accuracy of the roads and buildings damage maps were evaluated which are summarized in Table 6.

Table 5 indicates that, in the Bam dataset, the BDI index provided an OA of more than 84% and error rates lower than 16%. This index obtained promising results in three classes of intact or low-level damage buildings, high-level damage, and moderate-level damage but its performance in detecting low-level damaged buildings was less than 80%. Mainly, these errors originated from the definition of the thresholds for BDI in addition to some classification errors. Based on the presented numerical results in Table 5, the damage analysis by RDI provided an overall accuracy of more than 92%. The lowest accuracy belongs to the Moderate-Level blocked class with 50% producer accuracy while unblocked roads were detected with an accuracy of more than 93% that which indicates, this index may need more investigation for road damage analysis. In the Haiti dataset, the proposed method has provided better performance in the generation of multiple building damage compare to the Bam dataset, where the accuracy is more than 91% by OA index. It is worth mentioning that the accuracy of the road damage map of the Haiti dataset was lower than the Bam dataset. In this case, the high amount of shadows due to tall buildings may be one of the reasons.

4. Discussion

4.1. Performance of the proposed CNNs versus traditional ML methods

Classification is the most important step in damage/change detection algorithms. The visual and numerical analysis shown in our experiments proved that CNN models have higher performance compared to the traditional feature extraction and classification methods (based on the SVM and MLP, RF, and Xgboost classifiers using the Haralick features). It is noteworthy that since the CNN models in this work use the same MLP classifier, it is observed that the employed feature extraction is a significant factor in classification accuracy. Similar to the model proposed by Hao et al. (2018), our results showed that deep features outperform traditional ML algorithms for debris detection. This can be seen by comparing the results of damage detection based on texture features using MLP classification with the deep features by the same classifier. In this case, several falsely classified pixels were observed in the conventional classifiers using textural features.

Fig. 18 illustrates several sample buildings in the classified image showing the superiority of the designed CNN for debris detection in the B-DMG module in both datasets. Fig. 18-a shows intact buildings with IDs i, iii, and iv in the Bam dataset that is considered correctly by CNN using deep features while the results of the other methods include several false pixels. This CNN has also identified the debris areas in buildings with IDs ii, v, and vi correctly. As shown in Fig. 18b, the performance of the proposed method is compared with other methods. Accordingly, the proposed method has provided meaningful results in terms of classifying debris pixels from non-debris pixels. For instance, Fig. 18b with IDs i, ii, and iii shows damaged buildings that were detected by the proposed method as well as other methods providing many missed detection pixels. The proposed method also provides lower false pixels than other conventional methods of damage mapping (ii, v, and vi).

The classification results of the designed CNN in the R-DMG module in comparison with the other conventional classifiers based on textural features in the Bam and Haiti datasets are illustrated in Fig. 19a and 19b, respectively. As shown in these two figures, the use of conventional

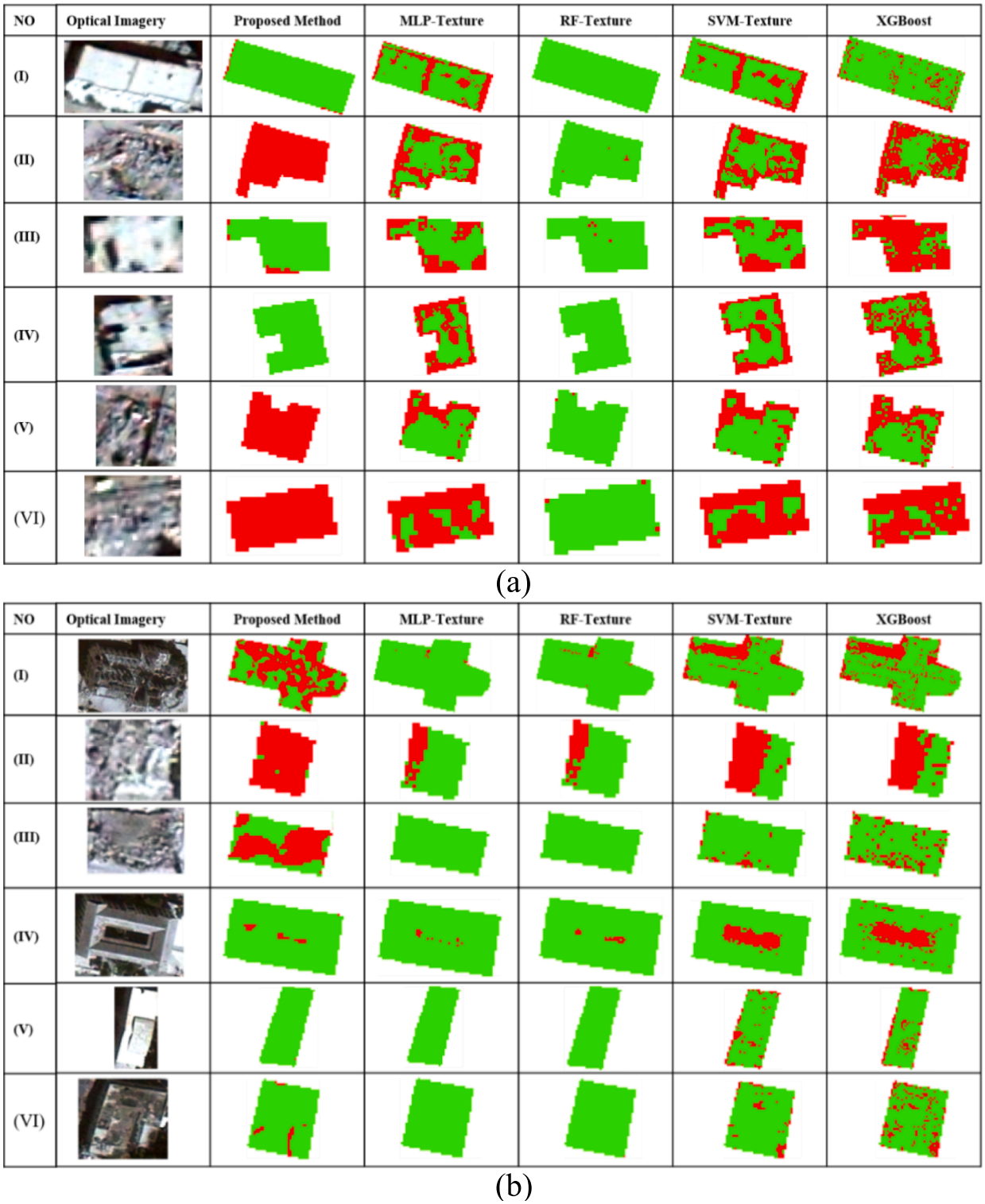

Fig. 18. Performance of the CNN in comparison with conventional classifiers in debris detection. (a) sample buildings in Bam dataset; (b) sample buildings in Haiti dataset;

classifiers based on texture features has missed various debris areas that have resulted in wrongly labeling many blocked roads as unblocked.

Table 6 summarizes the overall accuracies obtained for the classification of the optical high-resolution satellite imageries for damage assessment in comparison to our method. As can be seen from this table, our method outperformed traditional ML methods in both B-DMG and R-DMG purposes.

4.2. *Thresholding Multiple-Damage map*

The multiple-damage map is one of the most important achievements of this research. The BR-DMG can help to understand more details of damage maps that it can use as the basis map in the natural hazards. The multiple-damage map is generated in an unsupervised manner by thresholding RDI and BDI indices. The threshold value can be chosen as knowledge-based and depend on the view of the user against the damage

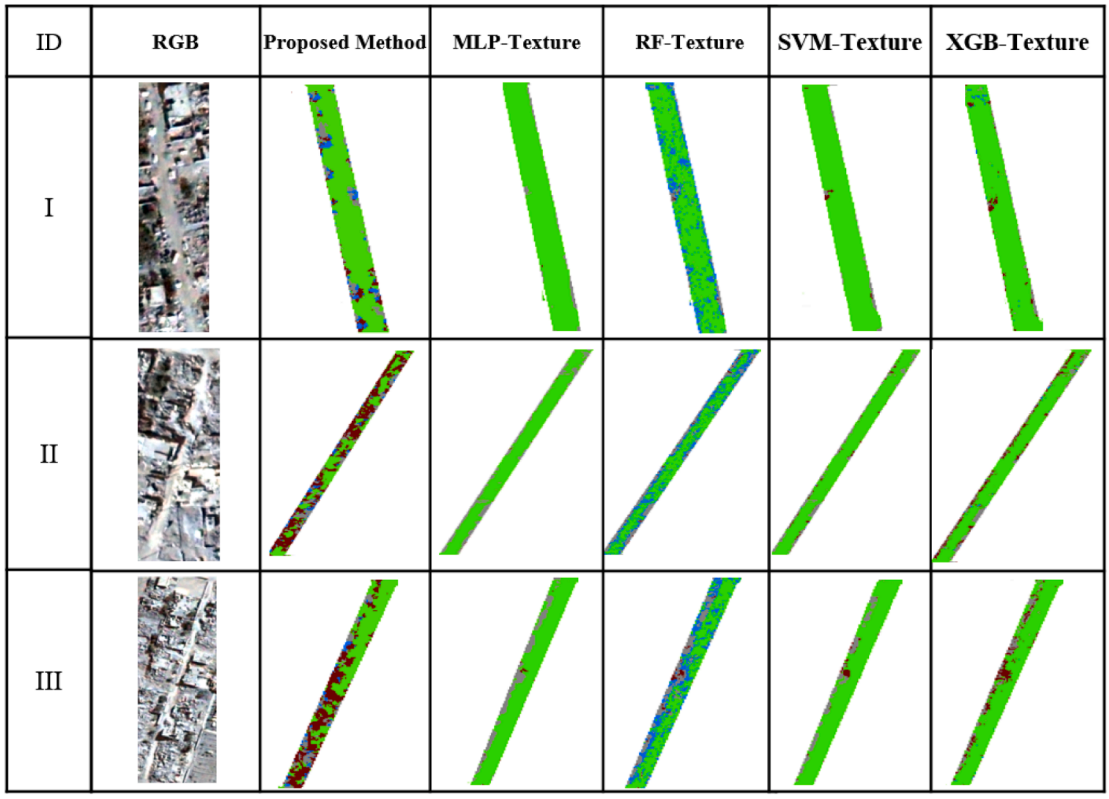

Fig. 19. Performance of the designed CNN in the R-DMG module in comparison with the conventional classifiers for debris detection. (a) three sample roads in the Bam dataset; (b) three sample roads in Haiti dataset.

Table 7
Comparison between the accuracies of the debris detection methods from high-resolution satellite images for buildings and roads.

		B-DMG		R-DMG	
Accuracy	Dataset	Multiple	Binary	Multiple	Binary
OA(%)	Bam	84.1	96.4	92.8	92.8
	Haiti	91.1	92.3	87.5	91.7

level. This research generated three levels of damage the threshold value has been chosen through a trial and error procedure. For as much as the damage map can be generated at the binary level, we examined the results of multiple damage maps at the binary level. Table 7 shows the BR-DMG results at the binary level. Based on the presented numerical results, the binary damage map generation has high accuracy compare to multiple damage maps. This issue originated from the thresholding in the generation of the multiple damage map.

4.3. Sample dataset

The availability of a suitable sample dataset is crucial for the success of damage mapping using DL-based methods. Semantic segmentation models, in particular, rely on a large amount of training data, which can be costly to acquire in practice. It is worth noting that architectures such as Swin-Unet, which are based on semantic segmentation, typically require a larger training dataset compared to shallower pixel-wise deep learning methods. These models need to process the entire set of pixels in the input images, which often results in a time-consuming process.

In contrast, the proposed framework in this study utilizes a sample dataset that is smaller than what is typically required for semantic segmentation-based models. Specifically, it was trained using only 33,000 samples for the Bam dataset. Furthermore, the proposed framework has the advantage of generating multiple damage maps in an unsupervised manner, while deep learning models often necessitate multiple sets of labeled damage data.

5. Conclusions

In this paper, a novel DL-based method for automatic map generation of building and road damage using post-earthquake optical high-resolution imagery was proposed. The debris detection module, which includes two different CNNs for buildings and roads, as compared with conventional classifiers, and both CNNs outperformed these classifiers. However, the accuracy of the designed CNN for debris detection in buildings was higher than the one for the road area, which may be due to the variety of existing objects inside the roads. Besides, the obtained results showed that the proposed novel indices for buildings and roads (termed BDI and RDI, respectively) were successful in evaluating the level of damage in buildings and the level of blockage in roads.

The proposed method has several advantages compared to other similar methods. They include: (1) The method provides simultaneously road and buildings damage maps; (2) The simple CNN architectures for debris detection require low computational cost; (3) Providing categorical degrees for building damage and road blockage; (4) Working with post-event satellite imagery without relying on pre-event imagery; (5) Utilizing the buildings damage map for validating the detected debris inside roads area in R-DMG module.

It is noted that the proposed method uses structural debris as the primary visual signature for determining building damage and road blockage. There are instances of structural damage or collapse patterns where debris is not significantly produced, despite the observed damage level at the ground level. For example, a collapsed building may still have a fallen, 'intact' structural roof. This inherent limitation can be attributed to the nature of space-borne imagery, which does not offer a vertical view of buildings. In such cases, the utilization of LiDAR data or stereo satellite images may prove to be helpful. Such remote sensing data with visual features coming from the elevational direction may be further beneficial to removing false-positive detection of debris. These potential improvements warrant our future work.

Declaration of Competing Interest

The authors declare that they have no known competing financial interests or personal relationships that could have appeared to influence the work reported in this paper.

Data availability

Data will be made available on request.

References

Bai, Y., Mas, E., Koshimura, S., 2018. Towards operational satellite-based damage-mapping using u-net convolutional network: A case study of 2011 tohoku earthquake-tsunami. Remote Sens. (Basel) 10, 1626.

Barzegar, F., Seydi, S., Farzaneh, S., Sharifi, M., 2023. Oil Spill Detection in the Caspian Sea with a SAR Image Using a Densenet Model. ISPRS Annals of the Photogrammetry, Remote Sensing and Spatial Information Sciences 10, 95–100.

Bellini, E., Nesi, P., Martelli, C., Gaitanidou, E., Archetti, F., Candelieri, A., Leuteritz, J.-P., Ferreira, P., Coconea, L., 2023. Building Resilient and Sustainable Cities Starting from the Urban Transport System. In: Urban Resilience: Methodologies, Tools and Evaluation: Theory and Practice. Springer, pp. 49–74.

Cooner, A.J., Shao, Y., Campbell, J.B., 2016. Detection of urban damage using remote sensing and machine learning algorithms: Revisiting the 2010 Haiti earthquake. Remote Sens. (Basel) 8, 868.

Erdogan, M., Yilmaz, A., 2019. Detection of building damage caused by Van Earthquake using image and Digital Surface Model (DSM) difference. Int. J. Remote Sens. 40, 3772–3786.

Hao, Y., Sun, G., Zhang, A., Huang, H., Rong, J., Ma, P., Rong, X., 2018. 3-D Gabor Convolutional Neural Network for Damage Mapping from Post-earthquake High Resolution Images, Advances in Brain Inspired Cognitive Systems: 9th International Conference, BICS 2018, Xi'an, China, July 7-8, 2018, Proceedings 9. Springer, pp. 139-148.

Coulibaly, I., Moslem Ouled, S., Richard L., Michèle. S.J., Mich'ele Saint-Jacques, 2015. Road Damage Detection From High Resolution Satellite Images Based on Machine Learning, multi-temp. IEEE 8th International workshop on the analysis of multi-temporal remote sensing images (MultiTemp 2015). Annecy, France.

Irwansyah, E., Gunawan, A.A.S., 2023. Deep Learning in Damage Assessment with Remote Sensing Data: A Review. Data Science and Algorithms in Systems: Proceedings of 6th Computational Methods in Systems and Software 2022, Vol. 2, 728-739.

Izadi, M., Mohammadzadeh, A., Haghighattalab, A., 2017. A new neuro-fuzzy approach for post-earthquake road damage assessment using GA and SVM classification from QuickBird satellite images. J. Indian Soc. Remote Sens. 45, 965–977.

Jia, S., Liao, J., Xu, M., Li, Y., Zhu, J., Sun, W., Jia, X., Li, Q., 2021. 3-D Gabor Convolutional Neural Network for Hyperspectral Image Classification. IEEE Trans. Geosci. Remote Sens.

Khodaverdizahraee, N., Rastiveis, H., Jouybari, A., Akbarian, S., 2020. Segment-by-segment comparison technique for generation of an earthquake-induced building damage map using satellite imagery. Int. J. Disaster Risk Reduct., 101505

Löfstedt, T., Brynolfsson, P., Asklund, T., Nyholm, T., Garpebring, A., 2019. Gray-level invariant Haralick texture features. PLoS One 14, e0212110.

Lu, J., Wu, H., Chen, D., 2023. Evaluation of collapse resistance of masonry-infilled RC frame building under blast loadings. Structures. 1126–1146.

Ma, H., Liu, Y., Ren, Y., Yu, J., 2020. Detection of collapsed buildings in post-earthquake remote sensing images based on the improved YOLOv3. Remote Sens. (Basel) 12, 44.

Mangalathu, S., Burton, H.V., 2019. Deep learning-based classification of earthquake-impacted buildings using textual damage descriptions. Int. J. Disaster Risk Reduct. 36, 101111.

Menderes, A., Erener, A., Sarp, G., 2015. Automatic detection of damaged buildings after earthquake hazard by using remote sensing and information technologies. Procedia Earth Planet. Sci. 15, 257–262.

Nex, F., Duarte, D., Tonolo, F.G., Kerle, N., 2019. Structural building damage detection with deep learning: Assessment of a state-of-the-art cnn in operational conditions. Remote Sens. (Basel) 11, 2765.

Rastiveis, H., Samadzadegan, F., Reinartz, P., 2013. A fuzzy decision making system for building damage map creation using high resolution satellite imagery. Nat. Hazards Earth Syst. Sci. 13, 455.

Rastiveis, H., Hosseini-Zirdoo, E., Eslamizade, F., 2015. Automatic blocked roads assessment after earthquake using high resolution satellite imagery. International Archives of the Photogrammetry, Remote Sensing & Spatial Information Sciences 40.

Saadat, M., Seydi, S.T., Hasanlou, M., Homayouni, S., 2022. A Convolutional Neural Network Method for Rice Mapping Using Time-Series of Sentinel-1 and Sentinel-2 Imagery. Agriculture 12, 2083.

Samadzadegan, F., Rastiveisi, H., Viii, W., 2008. Automatic detection and classification of damaged buildings, using high resolution satellite imagery and vector data. Int. Arch. Photogramm. Remote. Sens. Spat. Inf. Sci. 37, 415–420.

Samadzadegan, F., Zarrinpanjeh, N., 2008. Earthquake destruction assessment of urban roads network using satellite imagery and fuzzy inference systems. Int. Arch. Photogramm. Remote. Sens. Spat. Inf. Sci. 37, 409–414.
Shao, J., Tang, L., Liu, M., Shao, G., Sun, L., Qiu, Q., 2020. BDD-Net: a general protocol for mapping buildings damaged by a wide range of disasters based on satellite imagery. Remote Sens. (Basel) 12, 1670.
Taskin Kaya, G., Musaoglu, N., Ersoy, O.K., 2011. Damage assessment of 2010 Haiti earthquake with post-earthquake satellite image by support vector selection and adaptation. Photogramm. Eng. Remote Sens. 77, 1025–1035.
Tiwari, P.S., Pande, H., Gupta, S., Grover, C., Semwal, E., Agarwal, S., 2023. Damage Detection and Virtual Reconstruction of Built Heritage: An Approach Using High-Resolution Range and Intensity Data. J. Indian Soc. Remote Sens. 1–12.
Wang, J., Qin, Q., Zhao, J., Ye, X., Feng, X., Qin, X., Yang, X., 2015. Knowledge-based detection and assessment of damaged roads using post-disaster high-resolution remote sensing image. Remote Sens. (Basel) 7, 4948–4967.
Yang, B., Wang, S., Zhou, Y., Wang, F., Hu, Q., Chang, Y., Zhao, Q., 2020. Extraction of road blockage information for the Jiuzhaigou earthquake based on a convolution neural network and very-high-resolution satellite images. Earth Sci. Inf. 13, 115–127.
Zhang, A., Sun, G., Ma, P., Jia, X., Ren, J., Huang, H., Zhang, X., 2019. Coastal wetland mapping with Sentinel-2 MSI imagery based on gravitational optimized multilayer perceptron and morphological attribute profiles. Remote Sens. (Basel) 11, 952.
Zhou, Z., Gong, J., Hu, X., 2019. Community-scale multi-level post-hurricane damage assessment of residential buildings using multi-temporal airborne LiDAR data. Autom. Constr. 98, 30–45.